Chemical Science

ROYAL SOCIETY OF CHEMISTRY

EDGE ARTICLE

View Article Online
View Journal | View Issue

Cite this: *Chem. Sci.*, 2022, **13**, 11807

All publication charges for this article have been paid for by the Royal Society of Chemistry

Received 29th June 2022
Accepted 23rd September 2022

DOI: 10.1039/d2sc03640a

rsc.li/chemical-science

Green synthesis of water splitting electrocatalysts: IrO_2 nanocages *via* Pearson's chemistry†

Marine Elmaalouf,[a] Alexandre Da Silva,[a] Silvia Duran,[b] Cédric Tard,[b] Miguel Comesaña-Hermo,[a] Sarra Gam-Derouich,[a] Valérie Briois,[c] Damien Alloyeau,[d] Marion Giraud,[a] Jean-Yves Piquemal*[a] and Jennifer Peron*[a]

Highly porous iridium oxide structures are particularly well-suited for the preparation of porous catalyst layers needed in proton exchange membrane water electrolyzers. Herein, we report the formation of iridium oxide nanostructured cages, *via* a water-based process performed at room temperature, using cheap Cu_2O cubes as the template. In this synthetic approach, based on Pearson's hard and soft acid–base theory, the replacement of the Cu_2O core by an iridium shell is permitted by the difference in hardness/softness of cations and anions of the two reactants Cu_2O and $IrCl_3$. Calcination followed by acid leaching allow the removal of residual copper oxide cores and leave IrO_2 hierarchical porous structures with outstanding activity toward the oxygen evolution reaction. Fundamental understanding of the reaction steps and identification of the intermediates are permitted by coupling a set of *ex situ* and *in situ* techniques including *operando* time-resolved X-ray absorption spectroscopy during the synthesis.

1. Introduction

Iridium oxide (IrO_2) is the only electrocatalyst being active toward the oxygen evolution reaction (OER) and sufficiently stable to sustain the harsh conditions, highly oxidative and strongly acidic, existing at the anodes of proton exchange membrane water electrolysis (PEMWE) cells. For this reason and despite extensive research, IrO_2 is still the catalyst used in commercial devices, with loading contents approaching 2 mg cm^{-2}.[1,2] Nevertheless, due to its scarcity and high cost, its loading needs to be decreased while its activity and stability should be at least maintained and if possible, improved. The decrease in catalyst loading can be attained either by increasing the intrinsic activity of the catalysts by, for instance, modifying its composition (usually at the expense of its stability); or by preparing materials with extensive and accessible surface areas for the catalytic reaction. It is noteworthy that the use of electron conducting catalyst supports, such as high surface area carbons, is also prevented by the highly oxidative environment. Meanwhile, porosity is of the outermost importance given the necessity for high gas and water transport capabilities.

Porous IrO_2 thin films have shown promising properties.[3,4] However, while providing proof of performances and stability enhancement through a fine control of the material's architecture, synthetic methods leading to such structures are difficult to scale up and cannot be easily used to prepare porous catalyst layers to be deposited on the membrane and transferred into devices.

Hollow noble metal nanocatalysts can be fabricated *via* galvanic replacement,[5–9] Kirkendall effect, dealloying and selective etching.[10,11] Moreover, decreasing the noble metal content can be achieved by developing thin layers in the form of either core@shell or hollow nanoparticles. So-called Extended Surface Area (ESA) catalysts comprise large metal surfaces extended in two dimensions like thin films,[5] the high density of atomic steps and kinks providing more active sites for the catalytic reaction to occur. Electronic and/or strain effects caused by foreign atoms located in the inner layer or partially alloyed with the skin-catalyst particles are responsible for enhanced performance since they modify the chemisorption and reactivity of intermediates at the surface.[12–16] These particular structures have shown to be beneficial in fuel cells by making catalysts more resistant to surface area loss, providing long range conductivity and reduced mass transport losses.[17]

While these strategies have been widely applied in the past few years for fuel cells, only a few papers have been reported on the preparation of hollow Ir-based catalysts.[18–20] Ir–Ni@IrO_x core–shell NPs were prepared from $IrNi_x$ alloys by electrochemical Ni leaching and concomitant Ir oxidation,[20] while

[a]*Université Paris Cité, CNRS, ITODYS, F-75013 Paris, France. E-mail: jennifer.peron@u-paris.fr; jean-yves.piquemal@u-paris.fr*

[b]*Laboratoire de Chimie Moléculaire (LCM), CNRS, École Polytechnique, Institut Polytechnique de Paris, 91120 Palaiseau, France*

[c]*SOLEIL Synchrotron, UR1-CNRS, L'Orme des Merisiers, BP48, 91192 Gif-sur-Yvette, France*

[d]*Université Paris Cité, Laboratoire Matériaux et Phénomènes Quantiques (MPQ), F-75013 Paris, France*

† Electronic supplementary information (ESI) available. See https://doi.org/10.1039/d2sc03640a

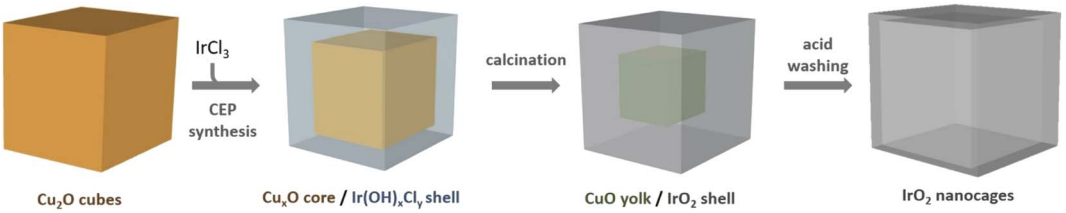

Fig. 1 Schematic representation of the 3-steps formation of IrO_2 nanocages from Cu_2O templates.

dodecahedral IrNi nanoframes were obtained using lanthanide metal-assisted synthesis.[21] Nanosegregation was also used to displace Ir at the surface of an IrFe alloy after thermal treatment under H_2/Ar,[22] or at the surface of IrRu alloys.[23] PdIr bimetallic octapods and nanocages were obtained by using Pd nanocubes as sacrificial template and subsequent co-reduction using a polyol (EG) with an Ir precursor.[24] Cobalt-doped IrCu octahedral nanocages showed lower overpotential compared to Ir/C nanocatalysts (0.293 *vs.* 0.315 V@10 mA cm^{-2}) and excellent stability.[19] Based on a modified galvanic replacement, Cu nanoparticles were used as template to prepare single-crystalline CuIr polyhedral nanocages at 250 °C. CuIr nanocrystals were obtained by the co-decomposition of Cu and Ir precursors at high temperature in oleylamine under CO atmosphere.[25] More recently, Cu@Ir core–shell particles were obtained in diphenylether/oleylamine.[26] Nevertheless, the high temperatures and overall harsh conditions needed lead to highly energy-consuming processes. Accordingly, and for obvious environmental and economic reasons, water-based syntheses are strongly preferable. By using water as the synthesis medium taking advantage of the aerosol process, we have also recently reported the preparation of highly porous IrO_2 and Ir-based mixed oxides and alloys catalysts from polymeric templates.[27–29]

Regarding water-based solution syntheses, the coordinating etching and precipitating (CEP) mechanism has been reported in the literature for the direct formation of porous oxides,[30] *e.g.* for producing SnO_2 boxes for lithium battery anodes with high lithium storage capacity.[29] This strategy inspired by Pearson's hard and soft acid–base concept (HSAB) has been applied for the production of hollow nanostructures of several transition metal oxides based on Fe,[32–34] Co,[32–36] Ni,[32,33,37,38] Zn,[33] Mn,[33] Sn,[31] and Ti.[39] To the best of our knowledge, this approach has never been implemented for the formation of noble metal-based oxides. In CEP syntheses, water or water/alcohol solutions are used as the synthetic medium and, Cu_2O nanostructures are typically used as templates because they are cheap, easy to synthesize and offer a wide variety of morphologies.[30,40] $S_2O_3^{2-}$ or Cl^- ions are in general added in the reaction medium to facilitate the displacement towards Cu_2O dissolution, and the reactions are performed in water/alcohol solution to control precursor hydrolysis and, as a consequence, the kinetics of the reaction. Nevertheless, this strategy has not been applied to produce hollow structures of noble metals since most of their cations are known to be soft acids, *i.e.* have comparable softness with Cu(I) ions, and therefore are not suitable for this replacement. Since Ir(III) ions present a harder character than other noble metal cations, they should permit hollow oxides to be obtained through CEP.[41] In this work, we extend this original strategy, performed in water and at room temperature, to obtain hollow IrO_2 nanocages in a three step process, by using Cu_2O nanocubes as sacrificial templates (Fig. 1). In the first step, $IrCl_3$ reacts with Cu_2O nanocubes to form a yolk shell structure in which precipitated Ir species surround a residual Cu_xO core. Subsequent calcination in air and acid leaching allow producing nanocages consisting of small isotropic IrO_2 nanoparticles that are highly active towards the OER. Besides producing highly porous architectures from cheap templates, this synthesis strategy is environmentally friendly since it is performed in water at room temperature.

2. Results and discussion

2.1. CEP synthesis of hydrous iridium hollow structures

According to Pearson's table,[41] Cu^+ ions present in Cu_2O show a softer character than Ir^{3+} ions (classified as "borderline") while O^{2-} is harder than Cl^-. For this reason, when Cu_2O nanoparticles interact with an aqueous solution of $IrCl_3$, Cu^+ ions will progressively be released to interact with Cl^- ions. Being unstable in aqueous solution, Cu^+ will also be rapidly oxidized into Cu^{2+}.[42] As the Cu_2O particles will dissolve, Ir^{3+} will interact with OH^- species resulting from the dissolution of Cu_2O. Following a CEP mechanism, and given that the appropriate conditions are met, $Ir(OH)_x$ species will precipitate as soon as they form, leading to the replacement of the initial Cu_2O nanocubes by $Ir(OH)_x$ nanocages.

To perform such synthesis, Cu_2O cubes reacted with $IrCl_3$, while using polyvinylpyrrolidone (PVP) to prevent the aggregation of the particles. The Cu_2O microparticles used as template hold a cubic cuprite structure with space group $Pn\bar{3}m$ as confirmed by XRD measurements (Fig. S1†). After 20 h of reaction, hollow structures preserving the original morphology of the initial Cu_2O cubes are obtained (Fig. 2a). We observe a 20% decrease in particle size from the initial *ca.* 320 nm edge length of the Cu_2O cubes to the final 265 nm ($\sigma = 6\%$) after CEP treatment. XRD analysis of the materials recovered after synthesis by centrifugation show a very broad peak between 30° and 50° characteristic of an amorphous phase, as well as several residual peaks characteristic of the initial Cu_2O template (Fig. S1†). X-ray photoelectron spectroscopy (XPS) analysis of the Cu species reveals the presence of mostly Cu(II) with a ratio Cu(I)/Cu(II) of 5/95 (Fig. S2†). Transmission electron microscopy

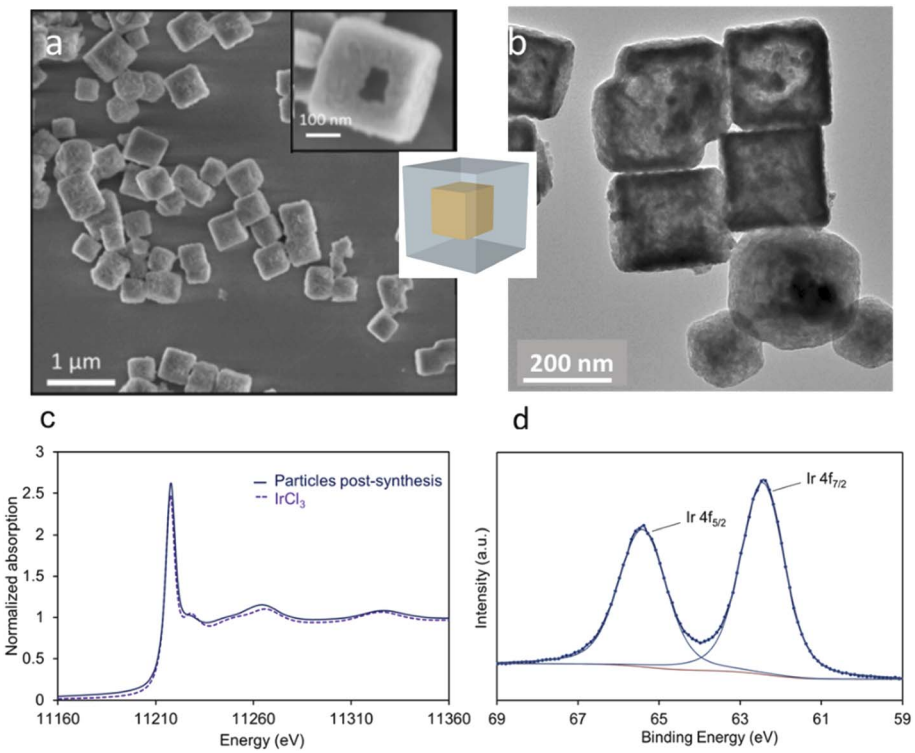

Fig. 2 (a) SEM and (b) TEM images of the particles recovered after synthesis. (c) Ir L_3 XANES spectrum of the particles recovered after synthesis and of the precursor $IrCl_3$. (d) XPS spectrum in the Ir 4f region of the particles recovered after synthesis.

(TEM) analyses show that the cages are made of a dense shell and a residual and more diffuse core, the latter being unstable under the electron beam (Fig. 2b). The Ir/(Ir + Cu) ratios obtained from scanning electron microscopy with energy dispersive X-ray analysis (SEM-EDX) and X-ray fluorescence (XRF) show that Ir represents *ca.* 20% of the total metal content in the resulting nanocage (Table 1).

The slightly higher amount of Ir detected by XPS, a surface sensitive technique, indicates that a higher amount of Ir is located on the surface of the nanocages. We can conclude that after the CEP reaction, the particles are made of an Ir-rich shell surrounding a residual core mostly made of hydrated Cu(II) species.

To discard a galvanic reaction between Ir^{3+} and Cu^{+}, and confirm a CEP mechanism, we have analyzed the oxidation state of Ir after reaction using X-ray absorption spectroscopy (XAS) and XPS (spectra in Fig. 2c and d, respectively). The XPS spectra obtained after CEP synthesis show the presence of only two peaks centered at 62.4 and 65.4 eV, corresponding to Ir $4f_{7/2}$ and Ir $4f_{5/2}$ signals from Ir(III). The absence of signatures at 60.9 eV and 63.9 eV indicate the absence of Ir(0) at the surface of the sample. The peak top position of the XANES spectra recorded at the Ir L_3-edge on post-synthesis material is measured at 11 218 eV and confirms the presence of Ir(III). The absence of Ir(0) discards a replacement through a galvanic reaction. This finding is a very important point since in the case of Pt for instance, Hong *et al.*[43] have shown that they are able to produce noble metal hollow structures from Cu_2O templates. But in their case, the resulting material is made of a PtCu alloy that results from a redox reaction between Pt and Cu cations. In the current mechanism, while Cu(I) is prone to oxidation in water, the transformation of Cu(I) into Cu(II) species does not induce Ir(III) reduction.

Table 1 Ir content in the particles recovered after synthesis. Standard deviations were calculated on four different samples for XRF and in five different zones of one sample for SEM-EDX analysis

	XRF	SEM-EDX	XPS
$\left(\frac{\text{Ir}}{\text{Cu}+\text{Ir}}\right)\%$, (SD)	19 (1.4)	18 (5.2)	26

2.2. *In situ* and *ex situ* study of the reaction kinetics

Several parameters had to be adjusted to allow for the formation of the hollow structure. Indeed, kinetics of both dissolution and precipitation processes have to be synchronous to preserve the template morphology and the Ir-based shell has to coat uniformly the surface of the template. PVP was needed in order to obtain well separated nanocubes. Unlike for syntheses performed with transition metals cations, the duration of the experiment in the case of Ir was found to be relatively long, *ca.* 20 h. Materials obtained at higher temperatures (30 °C or 60 °C) are made of IrO_2 particles that precipitate separately from the cubes (Fig. S3†), while higher $IrCl_3$ concentration (Ir/Cu 1.5 *vs.* Ir/Cl 0.5 in optimal conditions) leads to very fast dissolution of Cu_2O cubes without precipitation of Ir species.

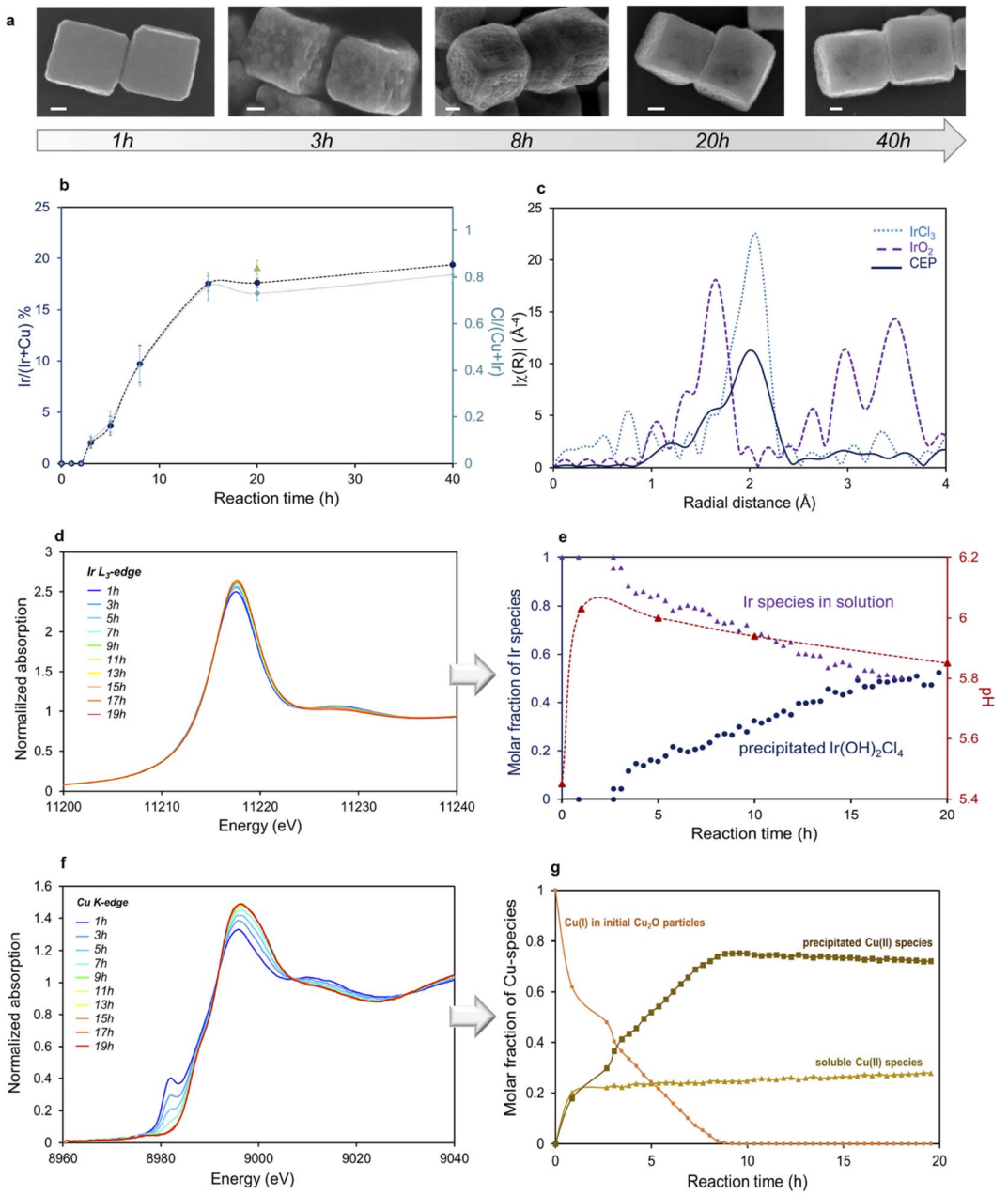

Fig. 3 (a) SEM images of the particles recovered after different reaction time (scale bars: 100 nm) and (b) corresponding EDX analysis of Ir and Cl content (SD error bars calculated in 3 different areas including several and/or isolated particles). (c) FT-EXAFS spectra of the particles after synthesis (labeled CEP), $IrCl_3$ and IrO_2 as references. (d) XANES spectra at the Ir L_3-edge recorded *in situ* as a function of reaction time and (e) molar fraction of precipitated Ir species and of soluble Ir(III) species in solution (violet triangles) determined by MCR-ALS from *in situ* XAS measurements (blue circles), and pH evolution as a function of time of reaction (red triangles). (f) XANES spectra at the Cu K-edge recorded *in situ* as a function of reaction time and (g) molar fraction of Cu species determined by MCR-ALS from *in situ* XAS measurements: initial cubes in orange circles, soluble Cu(II) species in light green triangles, precipitated amorphous Cu(II) species in olive squares.

To get better insight into the mechanisms of formation of these hollow structures, the replacement reaction was followed both by *ex situ* techniques analyzing the particles after different reaction times (SEM-EDX) and by *in situ* quick-XAS recorded simultaneously at both edges on the same solution. SEM images of the particles recovered after 1 h, 3 h, 8 h, 20 h, and 40 h of reaction are displayed in Fig. 3a. Corresponding Ir content compared to total metal content obtained from EDX analysis is plotted as a function of reaction time on Fig. 3b. After 1 h of reaction, we can already see that the surface of the Cu_2O cubes becomes slightly rough, while no Ir can be detected. After 3 h, the surface roughness is more pronounced and the Ir/(Ir + Cu) ratio detected in the cubes is 3%. As the reaction proceeds, the iridium content in the particle increases to reach a plateau of *ca.* 18 at% of Ir after 15 h. Subsequently, the surface recovers a smoother texture while internal voids are observed either from

broken particles or by contrast arising from SEM in lens imaging mode. The amount of Ir detected by EDX agrees with XRF analysis of the powder recovered after synthesis. Interestingly, the profile of Cl content, determined from EDX measurements (Fig. 3b) in the material follows that of Ir. To determine the nature of the precipitated Ir species, the final material recovered by centrifugation was analysed by XAS. Fourier transform (FT) of the Ir L_3-edge EXAFS spectra for the sample obtained after synthesis is plotted in Fig. 3c along with those of $IrCl_3$ in aqueous solution and IrO_2 as pellet used as references. On the FT-EXAFS spectra of $IrCl_3$, one peak characteristic of Ir–Cl distances is observed at $R' = 1.99$ Å (uncorrected for phase shift). On the FT-EXAFS spectra of IrO_2, the Ir–O characteristic peak is observed at $R' = 1.65$ Å, while further Ir–Ir distances are observed at *ca.* 3 and 3.5 Å.[27] Two contributions can be clearly observed in the CEP sample, one arising from Ir–Cl distances and a shoulder located at a shorter radial distance and characteristic of Ir–OH distances. From EXAFS fitting, the average number of Cl and OH neighbors can be determined; Ir(III) species are coordinated both with Cl and OH groups to form an $Ir(OH)_2Cl_4$ first coordination shell (Fig. S4 and Table S1†). A Cl/Ir ratio of *ca.* 4 obtained from SEM-EDX is in agreement with this formula (Fig. S5†).

The evolution of the different Ir and Cu species along the same reaction was also followed *in situ* by quick-XAS in a polyetheretherketone (PEEK) cell. XANES spectra recorded at the Ir L_3-edge and Cu K-edge and evolution of Ir and Cu molar fractions determined using multivariate curve resolution analysis (MCR-ALS) of the normalized XAS spectra as a function of reaction time are represented in Fig. 3d–g. Experimental details on MCR-ALS analysis for Ir and Cu are provided in Fig. S6 and S7,† respectively. We can observe in Fig. 3d that the rising edge position and the maximum of the white line of the XANES spectra do not vary with reaction time, confirming that Ir keeps its oxidation state (III) along the reaction. EXAFS fitting confirms that the Cl precursor evolves into a precipitated $Ir(OH)_2Cl_4$ species. The evolution of the molar fraction of $Ir(OH)_2Cl_4$ relative to total Ir species along the 20 h of reaction is shown in Fig. 3e. After an induction period of 3 h, similar to what was observed by SEM-EDX analysis, the molar fraction of $Ir(OH)_2Cl_4$ in the reaction medium increases to *ca.* 45% after 20 h. These results indicate that 45% of the iridium initially introduced in the reaction medium reacts to form $Ir(OH)_2Cl_4$. This value is in agreement with the one determined by X-ray fluorescence (XRF) analysis of both the supernatants and the particles obtained after 20 h. From these measurements we obtain a conversion rate of Ir into deposited species of 33.8% ($\sigma = 12.4\%$ calculated from 4 different reaction batches). $Ir(OH)_2Cl_4$ precipitates at the surface of residual copper oxide particles leading to a final Ir/(Ir + Cu) ratio of *ca.* 20%.

From MCR-ALS analysis applied to the series of XAS spectra recorded at the Cu K-edge (Fig. 3f) we can see that the initial Cu_2O is converted into two different species (Fig. 3g). Part of Cu_2O (*ca.* 30–40%) quickly dissolves into soluble $Cu(H_2O)_6^{2+}$ species. The remaining copper species (60–70%) arises from the evolution of solid state Cu_2O into amorphous Cu(II)-based solid in which Cu(II) ions are surrounded by 4 oxygen atoms, as determined by the fitting of the EXAFS spectra of the particles recovered after synthesis (Fig. S8 and Table S2†). These results seem to indicate that 60% of the initial Cu atoms remain in the final particles. Indeed, this calculation is confirmed by XRF analysis of both the supernatants and the particles obtained after 20 h of reaction. From these measurements we found that 42.6% ($\sigma = 14.4\%$) of Cu atoms are dissolved and recovered in the supernatant.

The plateau in Ir content in the final objects (Fig. 3b), equivalent to a maximal conversion rate, could possibly be attributed to the sluggish outwards diffusion of Cu atoms after the deposition of a certain amount of Ir species at the surface. Another explanation could be related to a restricted pH range in which the formation and precipitation of $Ir(OH)_2Cl_4$ species is possible. Accordingly, the pH of the solution was followed along the course of the experiment (Fig. 3e). We can see that the initial pH is slightly acidic due to the dissolution of the Ir precursor, followed by a progressive increase during the first 2.5 h of the reaction until reaching a value of *ca.* 6.1. After approximately

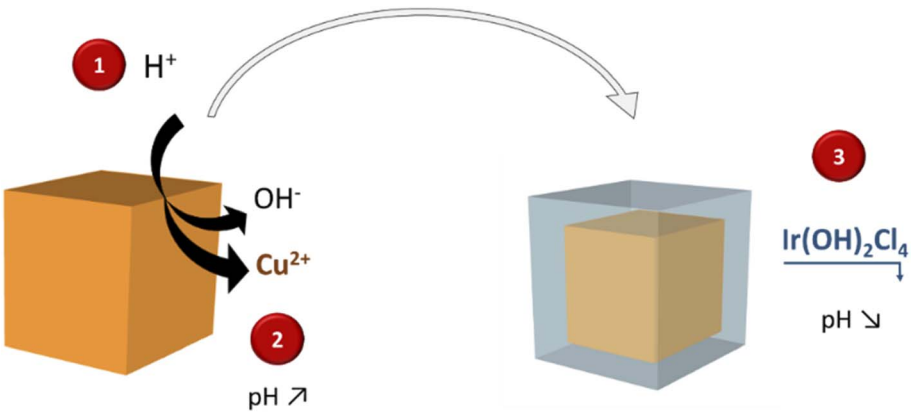

Fig. 4 Schematic representation of the CEP mechanism for the formation of $Ir(OH)_xCl_y$ from Cu_2O templates. Step 1: dissolution of Cu_2O cubes and release of Cu^{2+} and OH^-. Step 2: pH increases due to the release of OH^-. Step 3: the $Ir(OH_2)Cl_4$ forms and precipitate while OH^- is consumed and the pH decreases.

8 h, the pH starts to decrease, and by the end of the reaction (20 h) it reaches 5.8.

2.3. Mechanism of the reaction

All these observations have allowed us to propose a mechanism to explain the replacement reaction of Cu_2O nanocubes into Ir-based nanocages that is schematized in Fig. 4. In a first step, the slightly acidic pH induces partial dissolution of Cu_2O cubes into Cu(I) species that are very quickly oxidized into soluble Cu(II) species and OH^-. Indeed, Cu(I) in aqueous solution is not stable and rapidly oxidizes into Cu(II).[42] Within the first 3 h, the pH increases due to the release of OH^-, leading to an induction period in which no Ir is detected at the surface of the particles. Released OH^- react with the $IrCl_3$ to form $Ir(OH)_2Cl_4$, species that precipitate when a sufficiently high pH is reached. According to the Pourbaix diagram, when the pH increases above 5–6, the precipitation of $Cu(OH)_2$ is favored at the expense of soluble Cu(II) species. This explains why the amount of soluble Cu(II) ions quickly stabilizes at *ca.* 30% of the total Cu content (Fig. 3g). Subsequently, Cu_2O is further transformed into amorphous $Cu(OH)_2$ solid phase within the particle when the pH of the solution is high enough. Even though the solubility of $Cu(OH)_2$ is very low, the equilibrium established between solid $Cu(OH)_2$ and soluble Cu(II) species at this pH range allows the outwards diffusion of OH^-. The latter species immediately react with Ir precursors, producing the precipitation of a thicker $Ir(OH)_xCl_2$ layer that leads to a smoother particle's surface. Such reaction occurs until the diffusion of OH^- is impeded by the precipitated layer of $Ir(OH)_2Cl_4$ and/or until the pH becomes too low to allow the formation of the hydroxylated Ir complex.

2.4. Calcination

The Ir-based particles obtained after synthesis were calcined to convert the hydroxylated species into crystalline IrO_2 nanoparticles. Subsequently, the activity of the calcined material towards the water oxidation in acidic conditions was evaluated in a three-electrode electrochemical setup. Indeed, IrO_2 is the gold-standard catalyst for OER in acidic media due to its unmatched activity and stability. However, for such purpose, the calcination temperature to convert the Ir precursor into IrO_2 is of high importance since it is well known that amorphous iridium oxide materials or materials with very small crystallite size show higher electrochemical activity than their well-crystallized counterparts.[27,44–46] The optimal calcination temperature usually ranges between 400 °C and 500 °C, where the crystallisation of rutile IrO_2 occurs. Lower calcination temperature leads to unstable materials and higher one to larger crystals and lower activity.[28,47]

To convert hydroxylated Ir species into IrO_2, the as-synthesized materials were calcined from 400 to 550 °C for 15 min in a muffle furnace. X-ray diffractograms and corresponding crystallite size calculated by Rietveld refinement[48] are reported in Fig. S9.† We can see from XRD analysis that the material starts to crystallize above 400 °C. At 450 °C and above, peaks characteristic of IrO_2 are detected along with CuO peaks. Indeed, the residual amorphous Cu-containing phase is converted into the thermally-stable phase of CuO at 450 °C, leading to sharper peaks as the crystallite size increases with calcination temperature. At 450 °C we observe the appearance of IrO_2 diffractions, coming from crystallites with sizes below 2 nm. These objects increase to 2.3 nm then 2.8 nm when the temperature is increased to 500 °C and 550 °C, respectively. CuO crystallites are much larger and increase from 23 nm to 36 nm when the calcination temperature is increased from 450 °C to 550 °C. TEM images reveal a yolk shell structure in which small IrO_2 isotropic nanoparticles constitute the shell and large CuO particles are present in the internal void (Fig. S10†).

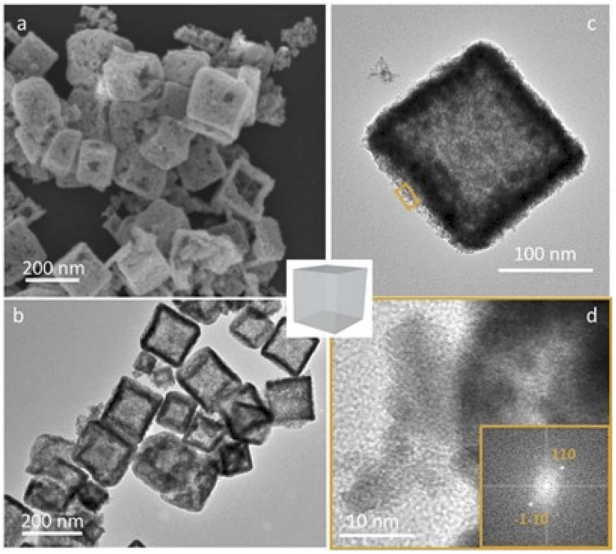

Fig. 5 (a) SEM, (b and c) TEM and (d) HR-TEM images of the particles recovered after synthesis, calcined at 550 °C and acid leached. The instet in (d) corresponds to the Fourier transform of the image on which the inter-reticular distances can be measured.

Subsequently, the particles were washed with a HCl aqueous solution to remove the non-noble metal oxide core and increase the inner porosity of the nanocages. We took profit from the solubility difference of Cu_2O (ref. 49) and IrO_x (ref. 50) phases in acidic media to remove selectively the copper oxide phase. Typical objects obtained after calcination at 550 °C and washed with acid are presented in Fig. 5. XRD confirms the disappearance of the CuO phase (Fig. S11†) and SEM and TEM images show hollow particles with a well-maintained morphology. While CuO is not detected anymore by XRD, XRF analyses of the washed particle give a residual Cu content of *ca.* 4 wt%. Electron diffraction obtained from HR-TEM images leads to an interplanar distance of 3.1 Å (Fig. 5d and S12†) which is in agreement with the theoretical value corresponding to (110) planes found in bulk IrO_2 (3.18 Å).

2.5. Activity of the nanocages towards the oxygen evolution reaction

The electrochemical activity toward the OER of the acid-leached nanocages calcined from 400 °C to 550 °C was evaluated in a three-electrodes electrochemical setup and compared to commercial IrO_2 as a reference. The current densities normalized to the actual mass of iridium are shown in Fig. 6a, and the

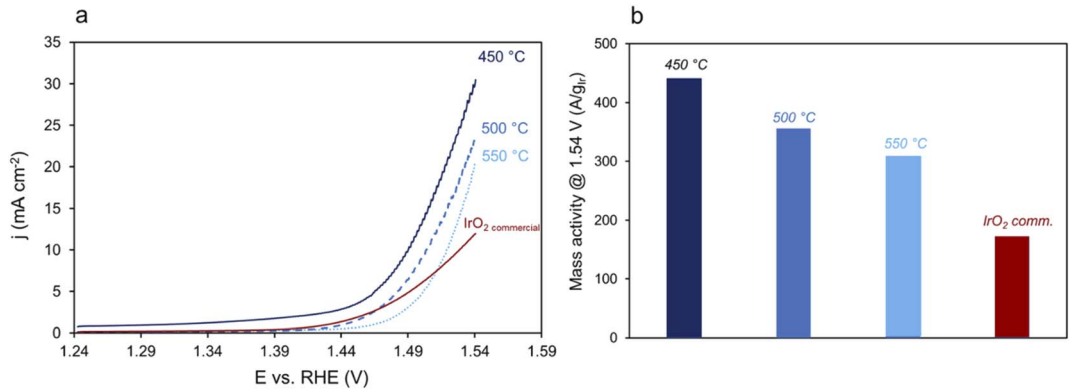

Fig. 6 (a) *IV* curves of the samples calcined at 450 °C, 500 °C and 550 °C and commercial IrO_2 and, (b) corresponding mass activities measured at 1.54 V and calculated using the actual mass of Ir in each sample. Experiments performed in H_2SO_4 0.05 M with a scan rate of 10 mV s^{-1} after conditioning (50 cycles between −0.2 and 1.2 V *vs.* SHE at 200 mV s^{-1}). Surface area of the electrode: 0.196 cm^2, total catalyst loading: 16 μg.

corresponding mass activity determined at 1.54 V in Fig. 6b. As expected, the activity decreases when the calcination temperature increases to 500 °C due to the crystallization of the materials. Nevertheless, the mass activity of the prepared catalysts is higher than commercial IrO_2 particles, whatever the calcination temperature. The mass activity of the IrO_2 cages calcined at 450 °C is of 450 A g_{Ir}^{-1}, *i.e.* more than two times higher than that of commercial IrO_2 particles. The surface area of the catalyst calcined at 550 °C, determined using mercury underpotential deposition,[51] was found to be of 37 m^2 g^{-1} which allows us to calculate a specific activity of 9 A m^2 for this catalysts, which is higher than that of commercial IrO_2 (6 A m^2). The very small size of IrO_2 nanoparticles and the high accessibility to catalytic sites allowed by the highly porous architecture lead to highly active materials. Correlation between the flexibility of the charge state of Ir cations, the presence of electrophilic oxygen and the Ir–O bonding characteristics,[52] but also the participation of lattice atoms down to 2 nm nanometers below the particle surface[53] have been suggested as key descriptors for both O_2 desorption and the adsorption of H_2O on iridium oxides. Even if their exact role is still poorly understood, the presence of a high number of surface metal atoms and the structure of nanoporous and amorphous/small-crystallites containing iridium oxides greatly improve the flexibility of the Ir charge states, promote the presence of electrophilic oxygens when compared to their crystalline counterparts and lead to high electrochemical activity towards the OER.[27,46]

3. Conclusion

In summary, we have developed a new synthetic strategy for the preparation of iridium oxide nanocages from cheap inorganic templates. The water-based synthesis, performed at room temperature, proceeds through a CEP mechanism as evidenced from XPS, SEM, and *in situ* and *ex situ* XAS experiments. Such multi-technique approach allows us to follow the transformation of Cu and Ir species along the reaction. After an induction period during which copper ions start to dissolve, hydroxylated-chlorinated iridium species precipitate at the surface of the cubes, forming a solid shell. After 20 h of reaction, core–shell structures made of Cu species surrounded by an Ir-rich shell are formed. The morphology of the material is well-suited to obtain hierarchical hollow structures in which ultra-small nanoparticles are assembled into hollow cages. Accordingly, the resulting materials can be easily converted into hollow IrO_2 nanocages, leading to electrocatalytic performances for the OER that are more than two times higher than those obtained with the commercial standard. Further work is ongoing to recycle the synthesis solution and reduce Ir precursor losses during the synthesis, as well as studying the stability of these highly active electrocatalysts in an electrolysis device.

4. Experimental section

4.1. Synthesis

$IrCl_3 \cdot xH_2O$ (98%) and commercial IrO_2 (Premion®) were purchased from Alfa-Aesar. All the other reactants were purchased from Sigma-Aldrich. In a typical synthesis, 90 mg of Cu_2O cubes are dispersed into 145 mL of mili-Q water along with 1 g of PVP (MW: 40 000 g mol^{-1}). After 1 h of mechanical stirring, 75 mL of a 9×10^{-3} M aqueous solution of $IrCl_3 \cdot xH_2O$ and 30 mL of a 0.43 M NaCl aqueous solution are added to the Cu_2O/PVP dispersion. The reaction medium is stirred at room temperature for the desired reaction time. The reaction is stopped by centrifugation of the solution at 22 000 rpm for 15 min. The particles collected after the first centrifugation are washed twice with a H_2O/EtOH (250/50 vol./vol.) mixture and once with pure ethanol. The greenish particles are then dried at room temperature under dynamic vacuum overnight. The samples are calcined in a muffle furnace from ambient temperature to the desired temperature with a heating ramp of 15 °C min^{-1}, and hold at the maximum temperature for 15 min. The particles are washed with a 0.5 M HCl solution for 15 min. The solution immediately turns dark blue. After 15 min the particles are recovered by centrifugation and washed twice with DI water.

4.2. Scanning electron microscopy (SEM)

SEM-EDX experiments were performed on a ZEISS Gemini SEM 360 equipped with an Oxford Instruments Ultim Max 170 mm^2

detector. SEM images and EDX mapping were obtained by Inlens SE detector (in column) at 5 kV accelerating voltage. Oxford Instrument AZtec software was used for the acquisition of EDX maps, point & ID analysis. For following the particles along the reaction, aliquots of the synthesis solution were samples after different times of reaction, centrifuged and the collected particles were dispersed in ethanol and deposited on silicium wafers and dried in air.

4.3. Transmission electron microscopy (TEM)

TEM images were obtained using a JEOL 2100 Plus transmission electron microscope operating at an acceleration voltage of 200 kV. Samples were prepared by depositing a drop of a diluted suspension of the nanoparticles in ethanol on a carbon-coated Cu grid.

4.4. X-ray diffraction (XRD)

XRD measurements were carried out using a Panalytical X'pert pro diffractometer equipped with a Co anode ($\lambda K_\alpha = 1.79031$ Å) and a multichannel X'celerator detector. All the diffractograms were fitted *via* MAUD program (Material Analysis Using Diffraction), a general X-ray diffraction program based mainly on the Rietveld refinement method,[48] and allowing determination of *a* and *c* parameters as well as the calculated crystallites sizes for each diffraction peak.

4.5. Energy dispersive X-ray fluorescence (EDXRF)

Elemental analyses of the powders were conducted by Energy Dispersive X-ray Fluorescence (EDXRF) using an epsilon 3XL spectrometer from Panalytical equipped with a silver X-ray tube. The calibration was performed by depositing a mass in the range 5–20 μg of the standard solution of each element on a polycarbonate membrane. The same conditions were adopted for all samples. The detection limits for Cu and Ir were determined to be 10 and 12 ng, respectively.

4.6. X-ray photoelectron spectroscopy (XPS)

XPS spectra were recorded using a K-Alpha+ spectrometer from Thermofisher Scientific, fitted with a microfocused, monochromatic Al K_α X-ray source ($h\nu = 1486.6$ eV; spot size = 400 micrometers). The pass energy was set at 150 and 40 eV for the survey and the narrow regions, respectively. Spectral calibration was determined by setting the main C1s (C–C, C–H) component at 285 eV.

4.7. Electrochemical characterization (OER protocol)

The potentiostat used for cyclic voltammetry was an Autolab PGSTAT 12, and ohmic drop was compensated in all cases (typically 30 Ω). The working electrode was a 5 mm diameter glassy carbon rotating disk electrode (Pine Instrument), carefully polished and ultrasonically rinsed in absolute ethanol before use. The counter electrode was a platinum wire and the reference electrode an aqueous saturated calomel electrode. All experiments were carried out in air at 10 mV s^{-1} and at a rotating rate of 1600 rpm. A 0.05 mol L^{-1} sulfuric acid solution (sulfuric acid, 0.1 N standardized solution, Alfa Aesar) was used as supporting electrolyte. From a mixture of 1 mg of synthesized material or iridium oxide (99.99%, Alfa Aesar), 2 mg of carbon Vulcan XC72R (Cabot), 250 μL of Nafion solution (5% w/w, Alfa Aesar) and 250 μL of deionized water (0.059 μS cm^{-2}), 8 μL of this suspension were deposited on the electrode surface, which was then dried in air and left for 30 min at 60 °C in an oven. Catalysts were then submitted to 50 cycles between −0.2 and 1.2 V *vs.* SHE at 200 mV s^{-1}, and the 50th forward scan recorded at 10 mV s^{-1} in 0.05 M H_2SO_4 is presented.

4.8. XAS/Quick-XAS

Cu K-edge and Ir L_3-edge X-ray absorption spectra were collected in the time-resolved Quick-XAS mode at the ROCK beamline (Synchrotron SOLEIL)[54] at a storage ring energy of 2.75 GeV and a nominal current of 500 mA. XAS measurements were carried out using the edge jumping capability of the Quick-XAS Si(111) channel-cut monochromator which allow to alternate measurements at both edges every 5 min with change of the Bragg angle of the monochromator and optimization of the stripes of harmonic rejection mirrors set at 2.8 mrad of grazing incidence. At the Cu K edge, B4C stripes were used whereas Pd ones were selected for harmonic rejection at the Ir L_3 edge. The frequency of oscillations of the monochromator was 2 Hz enabling to record a single XAS spectrum in 250 ms. For the whole measurements, XAS spectra were measured in transmission mode with three ionization chambers (IC) filled with nitrogen as X-ray detectors. Reference samples were measured either as pellets in boron nitride (15–20% wt. for Ir-based species and 3–4 wt% for Cu-based species) or as 20 mM aqueous dispersion or solution (based on metal content). Solution samples and *in situ* experiments were carried out in air, in homemade PEEK cells with an optical path of 6 mm. The conditions for the *in situ* experiments were similar to the synthesis conditions except that the reaction volume was reduced to *ca.* 2–2.5 mL. The concentrations were rather low and absorption edges intensities were below 0.1 for the two elements. In order to improve the S/N ratio, 600 spectra recorded consecutively with ascending Bragg angles were merged at each edge during the monitoring of the reaction. The reaction was carried out under vigorously stirring to avoid settling of the CuO_2 cubes. To this purpose, the cell was mounted on a stirring plate and the solution was stirred with spherical magnetic bars.

Prior data reduction and further analysis using the Athena software,[55] data merging and data normalization encompassing energy calibration and alignment were performed using the Graphical User Interfaces[56] available at the ROCK beamline for fast and massive handling of the Quick-EXAFS data. The energy was calibrated to the first inflection point of in the derivative spectra of the respective metal foil defined at 8979 eV for Cu and at 11 215 eV for Ir. Then the spectra were background corrected and normalized using NormalGui. The Cu absorption spectra were normalized using a linear function from 15 eV to 130 eV below the edge and a 2nd order polynomial function 35 eV to 800 eV above the edge, respectively. The Ir absorption spectra were normalized from 30 eV to 250 eV below the edge and 50 eV

to 1480 eV above the edge, respectively. Ir L_3-edge $k^3\chi(k)$ extracted EXAFS signals were Fourier transformed in *R*-space pseudo radial distribution functions using a Kaiser–Bessel window between $k_{min} = 3.0$ Å^{-1} and $k_{max} = 18$ Å^{-1} and *dk* window sill parameter equal to 1. Cu K-edge $k^3\chi(k)$ EXAFS signals collected were Fourier transformed in *R*-space pseudo radial distribution functions using a Kaiser–Bessel window between $k_{min} = 3.0$ Å^{-1} and $k_{max} = 14.4$ Å^{-1} and *dk* window sill parameter equal to 1. Extended X-ray Absorption Fine Structure (EXAFS) spectra were fitted using the Artemis program alternatively in *k* and *R* spaces and fitting windows are detailed in the caption below the tables.

4.9. Multivariate curve resolution analysis

Identification of the phases present during the *in situ* treatment using time-resolved XAS studies can be obtained using the MCR-ALS (multivariate curve regression with alternative least squares fitting) chemometric method.[57] The MCR-ALS minimization algorithm, developed under Matlab[58] was used herein for isolating, from the corresponding experimental data set, the spectra of the copper and iridium intermediate species formed over the course of the reaction. This method was also used to determine the speciation of both copper and iridium species as a function of time.

Data availability

The datasets supporting this article have been uploaded as part of the ESI.†

Author contributions

ME and ADS performed material synthesis, SD and CT performed electrochemical studies, MCH and DA performed TEM characterization and analysis, SGD performed SEM experiments, VB and MG performed and analysed synchrotron experiments, JYP and JP analysed XPS and XRD results, supervised the work, and wrote the manuscript.

Conflicts of interest

There are no conflicts to declare.

Acknowledgements

Philippe Decorse is gratefully acknowledged for XPS experiments, Ivonne Cocca and Sophie Nowak for XRF measurements. We acknowledge the ITODYS XRD, XPS-UPS and SEM facilities (Université Paris Cité, CNRS UMR 7086, Paris, France). The authors acknowledge financial support from the CNRS-CEA "METSA" French network (FR CNRS 3507) on the platform of Université Paris Cité. The XAS work was supported by a public grant overseen by the French National Research Agency (ANR) as a part of the "Investissements d'Avenir" program (ref: ANR-10-EQPX-45) provided for the building of the ROCK beamline, and by the Synchrotron SOLEIL proposal 20201546.

References

1 U. Babic, M. Suermann, F. N. Büchi, L. Gubler and T. J. Schmidt, *J. Electrochem. Soc.*, 2017, **164**, F387–F399.
2 M. Chatenet, B. G. Pollet, D. R. Dekel, F. Dionigi, J. Deseure, P. Millet, R. D. Braatz, M. Z. Bazant, M. Eikerling, I. Staffell, P. Balcombe, Y. Shao-Horn and H. Schäfer, *Chem. Soc. Rev.*, 2022, **21**, 4583–4762.
3 Y.-T. Kim, P. P. Lopes, S.-A. Park, A. Y. Lee, J. Lim, H. Lee, S. Back, Y. Jung, N. Danilovic, V. Stamenkovic, J. Erlebacher, J. Snyder and N. M. Markovic, *Nat. Commun.*, 2017, **8**, 1–8.
4 M. Bernicke, E. Ortel, T. Reier, A. Bergmann, J. Ferreira de Araujo, P. Strasser and R. Kraehnert, *ChemSusChem*, 2015, **8**, 1908–1915.
5 G. Ercolano, F. Farina, S. Cavaliere, D. J. Jones and J. Roziere, *J. Mater. Chem. A*, 2017, **5**, 3974–3980.
6 S. M. Alia, S. Pylypenko, K. C. Neyerlin, D. A. Cullen, S. S. Kocha and B. S. Pivovar, *ACS Catal.*, 2014, **4**, 2680–2686.
7 S. M. Alia, B. A. Larsen, S. Pylypenko, D. A. Cullen, D. R. Diercks, K. C. Neyerlin, S. S. Kocha and B. S. Pivovar, *ACS Catal.*, 2014, **4**, 1114–1119.
8 S. M. Alia, Y. S. Yan and B. S. Pivovar, *Catal. Sci. Technol.*, 2014, **4**, 3589–3600.
9 J. Zheng, D. A. Cullen, R. V. Forest, J. A. Wittkopf, Z. Zhuang, W. Sheng, J. G. Chen and Y. Yan, *ACS Catal.*, 2015, **5**, 1468–1474.
10 L. Zhang, L. T. Roling, X. Wang, M. Vara, M. Chi, J. Liu, S.-I. Choi, J. Park, J. A. Herron, Z. Xie, M. Mavrikakis and Y. Xia, *Science*, 2015, **349**, 412–416.
11 C. Chen, Y. Kang, Z. Huo, Z. Zhu, W. Huang, H. L. Xin, J. D. Snyder, D. Li, J. A. Herron, M. Mavrikakis, M. Chi, K. L. More, Y. Li, N. M. Markovic, G. A. Somorjai, P. Yang and V. R. Stamenkovic, *Science*, 2014, **343**, 1339–1343.
12 Y. Chen, F. Yang, Y. Dai, W. Wang and S. Chen, *J. Phys. Chem. C*, 2008, **112**, 1645–1649.
13 X. Wang, L. Zhang, S.-I. Choi, M. Luo, L. T. Roling, J. A. Herron, M. Mavrikakis, C. Ma, M. Chi, J. Liu, Z. Xie and Y. Xia, *Nat. Commun.*, 2015, **6**, 7594.
14 S. Alayoglu and B. Eichhorn, *J. Am. Chem. Soc.*, 2008, **130**, 17479–17486.
15 F. Zhao, B. Wen, W. Niu, Z. Chen, C. Yan, A. Selloni, C. G. Tully, X. Yang and B. E. Koel, *J. Am. Chem. Soc.*, 2021, **143**, 15616–15623.
16 J. Chen, P. Cui, G. Zhao, K. Rui, M. Lao, Y. Chen, X. Zheng, Y. Jiang, H. Pan, S. X. Dou and W. Sun, *Angew. Chem., Int. Ed.*, 2019, **58**, 12540–12544.
17 M. K. Debe, *Nature*, 2012, **486**, 43–51.
18 J. Park, T. Kwon, J. Kim, H. Jin, H. Y. Kim, B. Kim, S. H. Joo and K. Lee, *Chem. Soc. Rev.*, 2018, **47**, 8173–8202.
19 T. Kwon, H. Hwang, Y. J. Sa, J. Park, H. Baik, S. H. Joo and K. Lee, *Adv. Funct. Mater.*, 2017, **27**, 1604688.
20 H. N. Nong, H.-S. Oh, T. Reier, E. Willinger, M.-G. Willinger, V. Petkov, D. Teschner and P. Strasser, *Angew. Chem., Int. Ed.*, 2015, **54**, 2975–2979.

21 H. Jin, Y. Hong, J. Yoon, A. Oh, N. K. Chaudhari, H. Baik, S. H. Joo and K. Lee, *Nano Energy*, 2017, **42**, 17–25.
22 K. Sasaki, K. A. Kuttiyiel, D. Su and R. R. Adzic, *Electrocatalysis*, 2011, **2**, 134–140.
23 N. Danilovic, R. Subbaraman, K. C. Chang, S. H. Chang, Y. Kang, J. Snyder, A. P. Paulikas, D. Strmcnik, Y. T. Kim, D. Myers, V. R. Stamenkovic and N. M. Markovic, *Angew. Chem., Int. Ed.*, 2014, **53**, 14016–14021.
24 M. Liu, Y. Zheng, S. Xie, N. Li, N. Lu, J. Wang, M. J. Kim, L. Guo and Y. Xia, *Phys. Chem. Chem. Phys.*, 2013, **15**, 11822–11829.
25 D. Yoon, S. Bang, J. Park, J. Kim, H. Baik, H. Yang and K. Lee, *CrystEngComm*, 2015, **17**, 6843–6847.
26 A. C. Foucher, S. Yang, D. J. Rosen, J. D. Lee, R. Huang, Z. Jiang, F. G. Barrera, K. Chen, G. G. Hollyer, C. M. Friend, R. J. Gorte, C. B. Murray and E. A. Stach, *J. Am. Chem. Soc.*, 2022, **144**(17), 7919–7928.
27 M. Elmaalouf, M. Odziomek, S. Duran, M. Gayrard, M. Bahri, C. Tard, A. Zitolo, B. Lassalle-Kaiser, J.-Y. Piquemal, O. Ersen, C. Boissière, C. Sanchez, M. Giraud, M. Faustini and J. Peron, *Nat. Commun.*, 2021, **12**, 3935.
28 M. Faustini, M. Giraud, D. Jones, J. Rozière, M. Dupont, T. R. Porter, S. Nowak, M. Bahri, O. Ersen, C. Sanchez, C. Boissière, C. Tard and J. Peron, *Adv. Energy Mater.*, 2019, **9**, 1802136.
29 M. Odziomek, M. Bahri, C. Boissière, C. Sanchez, B. Lassalle-Kaiser, A. Zitolo, O. Ersen, S. Nowak, C. Tard, M. Giraud, F. Faustini and J. Peron, *Mater. Horiz.*, 2020, **7**, 541–550.
30 S. Sun and Z. Yang, *Chem. Commun.*, 2014, **50**, 7403–7415.
31 Z. Wang, D. Luan, F. Y. C. Boey and X. W. D. Lou, *J. Am. Chem. Soc.*, 2011, **133**, 4738–4741.
32 L. Yang, B. Zhang, W. Ma, Y. Du, X. Han and P. Xu, *Mater. Chem. Front.*, 2018, **2**, 1523–1528.
33 J. Nai, Y. Tian, X. Guan and L. Guo, *J. Am. Chem. Soc.*, 2013, **135**, 16082–16091.
34 J. H. Sohn, H. G. Cha, C. W. Kim, D. K. Kim and Y. S. Kang, *Nanoscale*, 2013, **5**, 11227–11233.
35 B. Qiu, Q. Zhu, M. Du, L. Fan, M. Xing and J. Zhang, *Angew. Chem., Int. Ed.*, 2017, **56**, 2684–2688.
36 X. Guan, J. Nai, Y. Zhang, P. Wang, J. Yang, L. Zheng, J. Zhang and L. Guo, *Chem. Mater.*, 2014, **26**, 5958–5964.
37 J. Nai, S. Wang, Y. Bai and L. Guo, *Small*, 2013, **9**, 3147–3152.
38 L. Tian, T. Yang, W. Pu and J. Zhang, *Nanoscale Res. Lett.*, 2019, **14**, 264.
39 Z. Wang and X. W. Lou, *Adv. Mater.*, 2012, **24**, 4124–4129.
40 Y. Shang and L. Guo, *Adv. Sci.*, 2015, **2**, 1500140.
41 R. G. Pearson, *J. Chem. Educ.*, 1968, **45**, 581–587.
42 B. Beverskog and I. Puigdomenech, *J. Electrochem. Soc.*, 1997, **144**, 3476–3483.
43 F. Hong, S. Sun, H. You, S. Yang, J. Fang, S. Guo, Z. Yang, B. Ding and X. Song, *Cryst. Growth Des.*, 2011, **11**, 3694–3697.
44 A. Minguzzi, C. Locatelli, O. Lugaresi, E. Achilli, G. Cappelletti, M. Scavini, M. Coduri, P. Masala, B. Sacchi, A. Vertova, P. Ghigna and S. Rondinini, *ACS Catal.*, 2015, **5**, 5104–5115.
45 V. Pfeifer, T. E. Jones, J. J. Velasco Velez, R. Arrigo, S. Piccinin, M. Havecker, A. Knop-Gericke and R. Schlogl, *Chem. Sci.*, 2017, **8**, 2143–2149.
46 S. Lee, Y. J. Lee, G. Lee and A. Soon, *Nat. Commun.*, 2022, **13**, 3171.
47 H. Jang and J. Lee, *J. Energy Chem.*, 2020, **46**, 152–172.
48 L. Lutterotti, S. Matthies and H.-R. Wenk, *IUCr: Newsletter of the CPD*, 1999, **21**, 14–15.
49 B. Beverskog and I. Puigdomenech, *J. Electrochem. Soc.*, 1997, **144**, 3476–3483.
50 R. Zhang, N. Dubouis, M. Ben Osman, W. Yin, M. T. Sougrati, D. A. D. Corte, D. Giaume and A. Grimaud, *Angew. Chem., Int. Ed.*, 2019, **58**, 4571–4575.
51 S. Duran, M. Elmaalouf, M. Odziomek, J.-Y. Piquemal, M. Faustini, M. Giraud, J. Peron and C. Tard, *ChemElectroChem*, 2021, **8**, 3519–3524.
52 A. Lončar, D. Escalera-López, S. Cherevko and N. Hodnik, *Angew. Chem., Int. Ed.*, 2022, **61**, e202114437.
53 K. Schweinar, B. Gault, I. Mouton and O. Kasian, *J. Phys. Chem. Lett.*, 2020, **11**, 5008–5014.
54 V. Briois, C. La Fontaine, S. Belin, L. Barthe, T. Moreno, V. Pinty, A. Carcy, R. Girardot and E. Fonda, *J. Phys.: Conf. Ser.*, 2016, **712**, 012149.
55 B. Ravel and M. Newville, *J. Synchrotron Radiat.*, 2005, **12**, 537–541.
56 C. Lesage, E. Devers, C. Legens, G. Fernandes, O. Roudenko and V. Briois, *Catal. Today*, 2019, **336**, 63–73.
57 W. H. Cassinelli, L. Martins, A. R. Passos, S. H. Pulcinelli, C. V. Santilli, A. Rochet and V. Briois, *Catal. Today*, 2014, **229**, 114–122.
58 J. Jaumot, R. Gargallo, A. de Juan and R. Tauler, *Chemom. Intell. Lab. Syst.*, 2005, **76**, 101–110.